Electronic Supplementary Material (ESI) for Physical Chemistry Chemical Physics.

Structure and magnetism of electrospun porous high-entropy $(Cr_{1/5}Mn_{1/5}Fe_{1/5}Co_{1/5}Ni_{1/5})_3O_4$, $(Cr_{1/5}Mn_{1/5}Fe_{1/5}Co_{1/5}Zn_{1/5})_3O_4$ and $(Cr_{1/5}Mn_{1/5}Fe_{1/5}Ni_{1/5}Zn_{1/5})_3O_4$ spinel oxide nanofibers

Alessandro Ponti,*[a] Claudia Triolo,[b,c] Beatrix Petrovičovà,[b] Anna M. Ferretti,[a] Gioele Pagot,[d] Wenlei Xu,[e] Vito Di Noto,[d] Nicola Pinna*[e] and Saveria Santangelo*[b,c]

[a] Laboratorio di Nanotecnologie, Istituto di Scienze e Tecnologie Chimiche "Giulio Natta" (SCITEC), Consiglio Nazionale delle Ricerche, Via Fantoli 16/15, 20138 Milano, Italy.
[b] Dipartimento di Ingegneria Civile, dell'Energia, dell'Ambiente e dei Materiali (DICEAM), Università "Mediterranea", Loc. Feo di Vito, 89122 Reggio Calabria, Italy.
[c] National Reference Center for Electrochemical Energy Storage (GISEL), Consorzio Interuniversitario Nazionale per la Scienza e Tecnologia dei Materiali (INSTM), 50121 Firenze, Italy.
[d] Section of Chemistry for the Technology (ChemTech), Department of Industrial Engineering, University of Padova, Via Marzolo 9, 35131 Padova (PD), Italy.
[e] Institut für Chemie and IRIS Adlershof, Humboldt-Universität zu Berlin, Brook-Taylor Str. 2, 12489 Berlin, Germany.

Supporting Information

Supporting Information includes a scheme of the spinel lattice and additional details on synthesis, morphology and surface composition of the HESO-NFs, phase purity of the oxide and inversion degree of the spinel phase, results of Rietveld refinements, fitting of high-field magnetization to a saturation approach model, and calculation of the Helmholtz free energy for cation distributions.

Spinel lattice

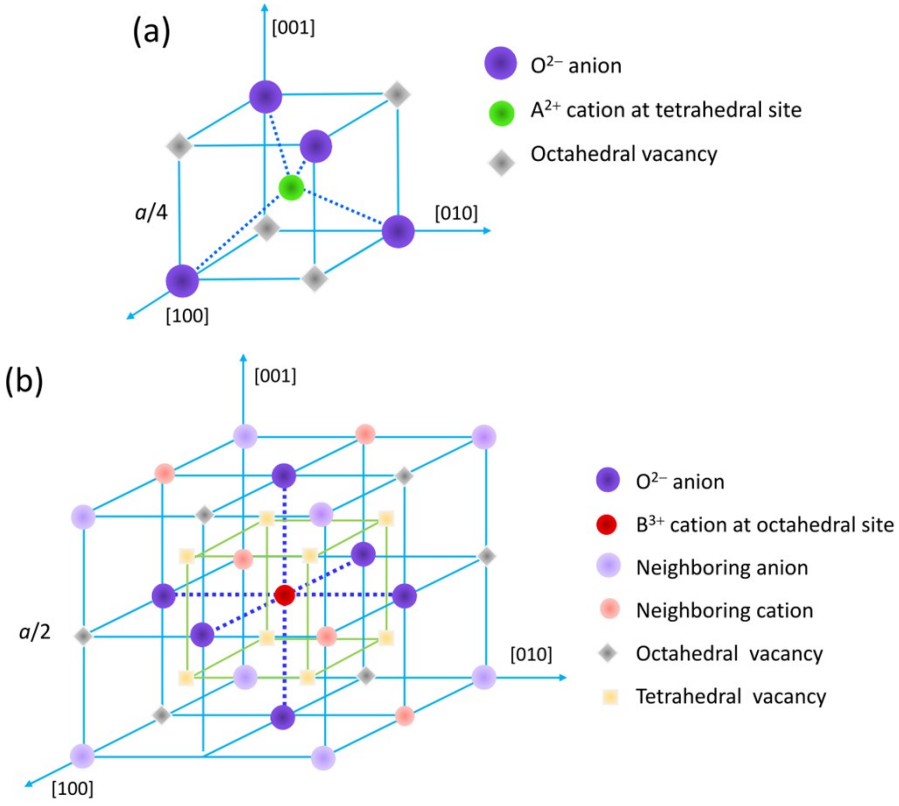

Fig. S1 Schematic drawings of cations occupying (a) tetrahedral and (b) octahedral sites in the $A^{(II)}B^{(III)}{}_2O_4$ *normal* spinel lattice and their nearest neighbors (inspired to ref. 1).

Experimental Section

Reagents and chemicals.

The following reagents were utilized as transition metal (TM) sources for the synthesis of (Cr,Mn,Fe,Co,Ni), (Cr,Mn,Fe,Co,Zn) and (Cr,Mn,Fe,Ni,Zn) HESO-NFs: chromium (III) acetate hydroxide, $Cr_3(OH)_2(CH_3COO)_7$ (purity: 98%; CAS No. 39430-51-8, Sigma Aldrich, Burlington, MA, USA), manganese(II)acetate tetrahydrate, $Mn(CH_3COO)_2{\cdot}4H_2O$ (purity: 99%; CAS No. 6156-78-1, Sigma Aldrich), iron (II) acetate, $Fe(CH_3COO)_2$ (purity 95%; CAS No. 3094-87-9 Sigma Aldrich), cobalt (II) acetate tetrahydrate, $Co(CH_3COO)_2{\cdot}4H_2O$ (purity: 99%; CAS No. 6147-53-1, Sigma Aldrich), nickel (II) acetate tetrahydrate, $Ni(CH_3COO)_2{\cdot}4H_2O$ (purity: 98%; CAS No. 6018-89-9, Sigma Aldrich), zinc (II) acetate dehydrate, $(CH_3COO)_2Zn{\cdot}2H_2O$ (purity: 98%; CAS No. 5970-45-6, Fischer Scientific, Hampton, NH, USA).

The precursor solutions were prepared via sol-gel method by using polyacrylonitrile, $(C_3H_3N)_n$ (average molecular weight: 150000 g mol^{-1}; purity: 99.9%; CAS No. 25014-41-9, Sigma Aldrich), and *N,N*-dimethylformamide, $HCON(CH_3)_2$ (anhydrous: 99.8%; CAS No. 68-12-2, Sigma Aldrich), as a polymer and a solvent, respectively.

Synthesis of the HESO-NFs.

The HESO-NFs were prepared by electrospinning (ES), followed by calcination (Figure S2). In a typical synthesis, 0.325 g polyacrylonitrile (PAN) was dissolved in 4.550 g *N,N*-dimethylformamide (DMF) and the resulting solution was magnetically stirred at room temperature (RT) until it became clear. Then, proper amounts of the reagents (Table S1) were added, one at a time (Figure S2a), under continuous stirring in order to obtain a homogeneous spinnable solution containing the selected equimolar combination of five transition metals (Figure S2b). After slow mixing overnight at RT, the solution was loaded into a 20 mL syringe equipped with a 40 mm long 0.8 mm gauge stainless steel needle. Electrospinning (Figure S2c) was operated via a CH-01 Electro-spinner 2.0 (Linari Engineering s.r.l.) by feeding solution at 23.5 µL min^{-1} rate. The NFs ejected from the needle under an applied DC voltage of 15 kV were collected over an 11 cm distant grounded aluminum foil. After drying at RT overnight to remove the DMF residuals, the as-spun nonwoven fibrous membrane was peeled from the collector and calcined in static air at 973 K for 2 h and at 1173 K for 2 h (Figure S2d). During calcination, temperature was increased at a fast rate (10 K min^{-1}) in order to obtain mostly hollow NFs consisting of interconnected oxide nanograins.[2]

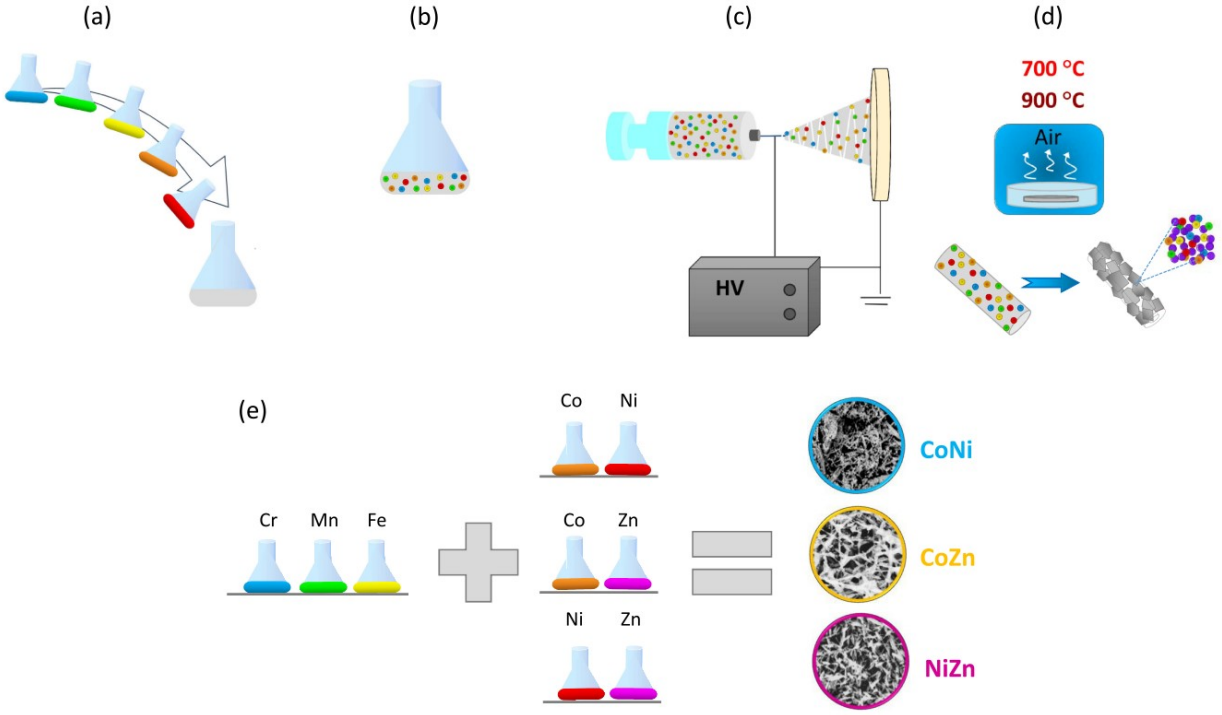

Fig. S2 (a–d) Schematic description of the experimental procedure followed to synthesize the HESO-NFs: (a) addition of the selected reagents, one at a time, to the PAN/DMF solution; (b) spinnable solution containing an equimolar combination of five TMs; (c) electrospinning; (d) calcination and obtainment of hollow NFs consisting of interconnected HEO nanograins from their precursors. (e) Selected equimolar combinations of TMs and codes of the HESO-NFs correspondingly obtained.

Table S1. Amount of reagents dissolved in the PAN/DMF solution in order to obtain spinnable solutions containing three different equimolar combinations of transition metals, namely (Cr,Mn,Fe,Co,Ni), (Cr,Mn,Fe,Co,Zn) and (Cr,Mn,Fe,Ni,Zn).

Reagent	Amount / g
Chromium (III) acetate hydroxide	0.0881
Manganese (II) acetate tetrahydrate	0.1078
Iron (II) acetate	0.0765
Cobalt (II) acetate tetrahydrate	0.1096
Nickel (II) acetate tetrahydrate	0.1095
Zinc (II) acetate dihydrate	0.0966

Physicochemical characterization.

Morphology. The morphology, texture, microstructure, crystalline phase and surface composition of the as-calcined HESO-NFs were investigated by scanning electron microscopy (SEM), transmission electron microscopy (TEM), x-ray diffraction (XRD), micro-Raman spectroscopy (MRS) and x-ray photoelectron spectroscopy (XPS). The SEM images and elemental maps were acquired by a Phenom Pro-X scanning electron microscope equipped with an energy-dispersive X-ray (EDX) spectrometer. High-resolution TEM (HRTEM), high-angle annular dark-field scanning transmission electron microscopy (HAADF-STEM), selected-area electron diffraction (SAED) and energy dispersive x-ray spectroscopy (EDX) elemental mappings were carried out on a FEI Talos F200S scanning/transmission electron microscope, operated at 200 kV. In order to get more detailed information on the NF inner morphology, projection analysis of STEM-EDX maps was carried out. Projection analysis consists in selecting a straight, constant-diameter NF (or region of a NF) and integrate (project) the map intensity along the NF axis. Then, the resulting transverse projection is fitted to models appropriate for solid or hollow NFs, namely

$$I_{solid} = I_{background} + I_0\sqrt{1-(r/R)^2},$$

$$I_{hollow} = I_{background} + I_0\left(\sqrt{1-\left(r/R_{out}\right)^2} - \sqrt{1-\left(r/R_{in}\right)^2}\right),$$

where $I_{background}$ is the projected background intensity, I_0 is a constant depending on the NF size and composition, r is the distance from the NF axis, R is the radius of a solid NF, and R_{out} and R_{in} are the outer and inner diameter of a hollow NF, respectively. Comparing how well the NF projections fit to the models, one can get some insight into the NF internal structure. The projections were obtained from oxygen STEM/EDX maps by integrating NF segments of length 300 to 2500 nm.

To collect structural information about the primary particles, the geometrical phase analysis (GPA) of lattice fringes proposed by Hÿtch[3] was applied to HRTEM images. In brief, the HRTEM image was Fourier transformed (FT), and the peaks were assigned to the reciprocal vectors $\mathbf{g}_{hkl}$ of the spinel lattice. For each peak of interest, the 2D FT image was filtered by an isotropic Gaussian filter and inverse FT-ed to real space as a complex image. The intensity ($Re^2 + Im^2$) image highlights the regions of the HRTEM image where the $\mathbf{g}_{hkl}$ fringes are present. The phase of the complex image was further processed following ref. 4 to produce the lattice rotation and Lagrange strain maps, corresponding to $\mathbf{g}_{hkl}$. The GPA results are presented in three separate images: (i) the fringe-intensity-colored TEM image, *i.e.,* the original black-and-white HRTEM image colorized with yellow hue proportional to the lattice fringe amplitude; (ii) the rotation map, expressed as rotation in degree from $\mathbf{g}_{hkl}$; (iii) the Lagrange strain map, expressed as percentage deviation of the imaged interplanar distance from $1/|\mathbf{g}_{hkl}|$.

Crystalline phase of the oxide, phase purity and crystallinity of HESO-NFs. XRD analysis was carried out with a Bruker D2 diffractometer using Ni β-filtered Cu-K_α radiation source (λ = 0.1541 nm). A NTEGRA—Spectra SPM NT-MDT confocal microscope coupled to a solid-state laser operating at 2.33 eV (532 nm) was utilized to measure Raman scattering. Spectra were recorded in air at RT. The use of a low laser power (250 μW at the sample surface) prevented local heating. The scattered light from the sample, collected by means of a 100X Mitutoyo objective (NA = 0.75), was detected by a cooled ANDOR iDus CCD Camera. The spatial homogeneity of the samples was evaluated by recording spectra from several random positions on each specimen. The average of the collected spectra provided a reliable picture of the entire sample. Further details on the instrumentation can be found in ref. 2

Surface composition of HESO-NFs and oxidation states of cations. The XPS studies were performed at RT working at a pressure of *ca*. 10^{-6} mbar by using an EnviroESCA (Specs) instrument equipped with an Al-K_α excitation source ($h\upsilon$ = 1486.6 eV). Survey spectra were acquired at 100 eV pass energy, 1.0 eV·step^{-1}, and 0.1 sec·step^{-1}. High-resolution curves were obtained at 50 eV pass energy, 0.1 eV·step^{-1}, and 0.1 s·step^{-1}. In agreement with the literature,[5] binding energy values (BE; uncertainty = ± 0.2 eV) were corrected for charging assigning to the adventitious C 1*s* peak, attributed to adventitious hydrocarbons, the value of 284.8 eV. XPS spectra were fitted using the Keystone software of Specs and applying a Shirley-type background function.[6] The sensitivity factors of integrated peak areas used for atomic percentages (at. %) quantification were supplied by Specs.

Magnetic properties. The magnetic properties of the NFs were measured by a Quantum Design MPMS XL-5 SQUID magnetometer. Weighted amounts of NFs were tightly wrapped in Teflon tape. Since room temperature reversibility was not expected, each experiment was carried out using a fresh NF specimen from the same batch. All magnetization data were corrected for the diamagnetism of the Teflon tape and were scaled to the specimen mass. Zero-field cooled (ZFC) and field-cooled (FC, H_{cool} = 100 Oe) magnetization were measured between 5 and 300 K (400 K for CoNi) using H_{meas} = 100 Oe. Magnetization isotherms

(hysteresis loops) were measured between ±50 kOe at several temperatures ranging from 5 to 300 K. Because constant magnetization could not be reached at 50 kOe and a significant linear magnetization component was present, we fitted the approach to saturation model for ferrimagnetic powders[7] $M = M_{sat}(1–A/H–B/H^2) + \chi_p H$ to the high field (≥ 10 kOe) data to measure the saturation magnetization M_{sat} and the high-field linear (paramagnetic) susceptibility χ_p. It turned out that the B/H^2 term was not statistically significant and good fits were obtained with the simpler formula $M = M_{sat}(1–A/H) + \chi_p H$. The fit results can be found in the supporting information. The high field magnetization M_{50k} (H = 50 kOe) and remanence M_{rem} (after saturation at 50 kOe) were independently measured between 5 and 300 K with a smaller temperature step.

Morphology of the HESO-NFs

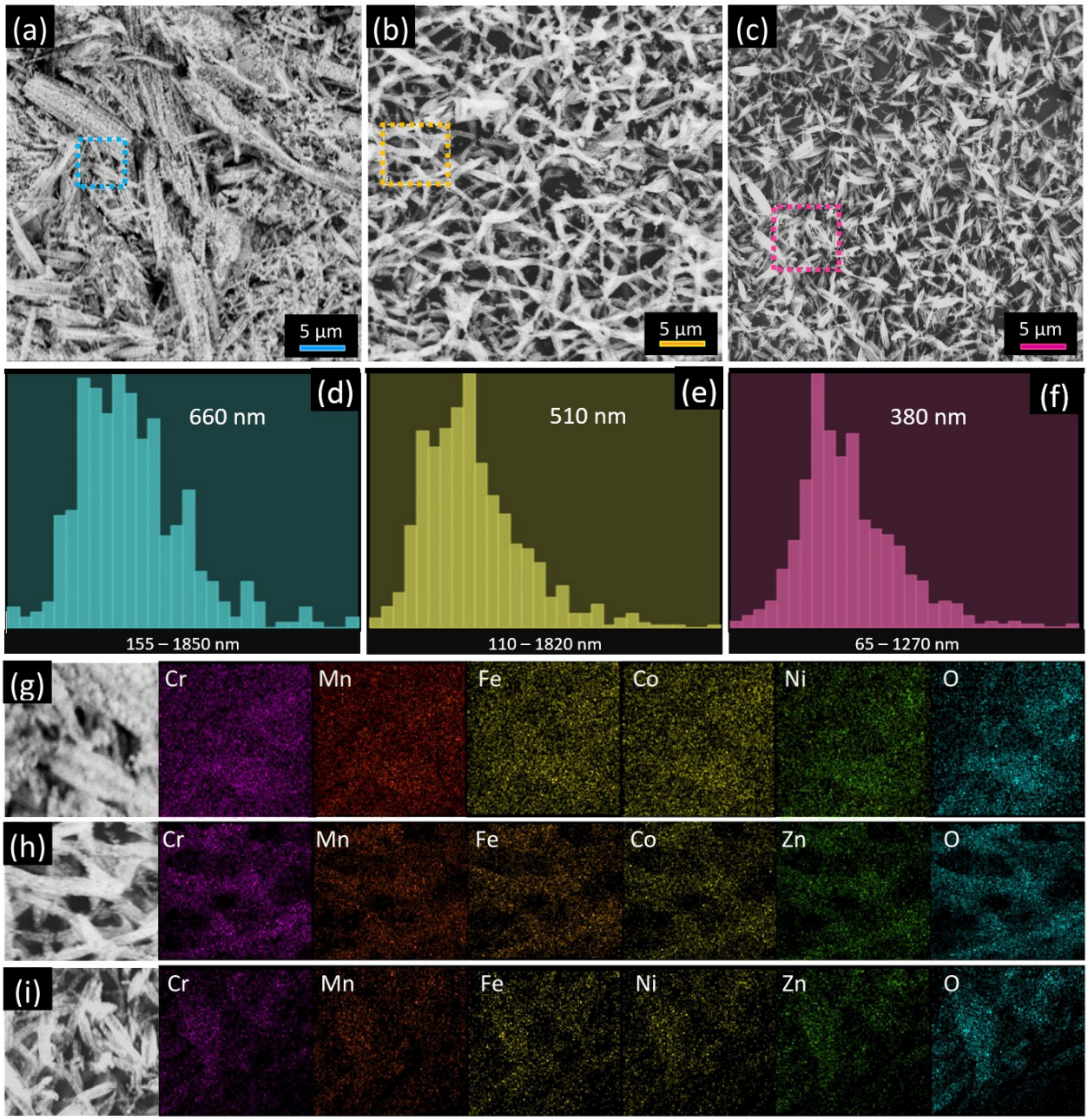

Fig. S3 Results of the SEM/EDX analysis on samples (a,d,g) CoNi, (b,e,h) CoZn and (c,f,i) NiZn. (a–c) SEM images; (d–f) NF diameter distribution, as obtained by Fibermetric software from the SEM images; (g–i) elemental maps.

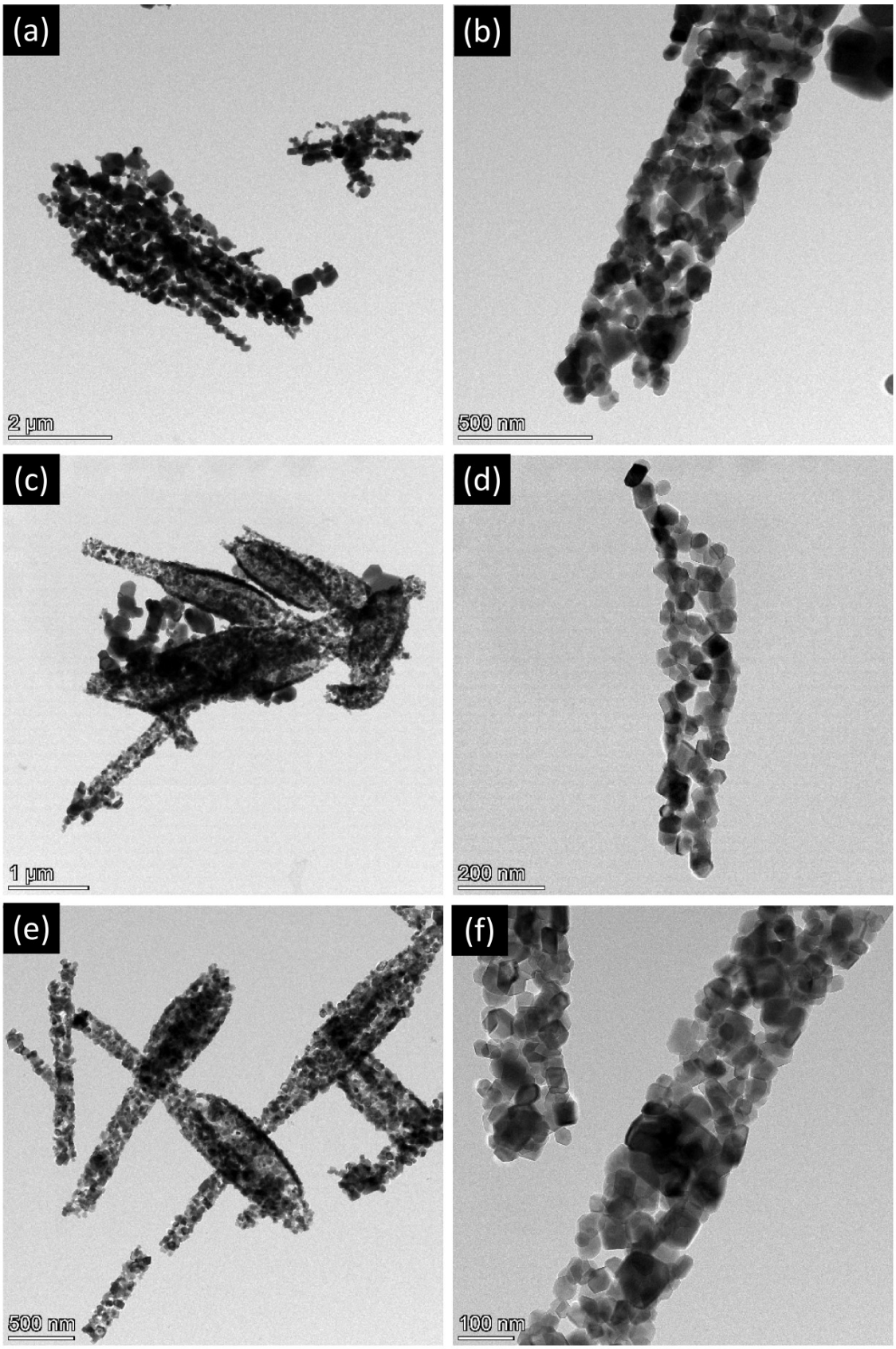

Fig. S4 TEM images of samples (a,b) CoNi, (c,d) CoZn and (e,f) NiZn.

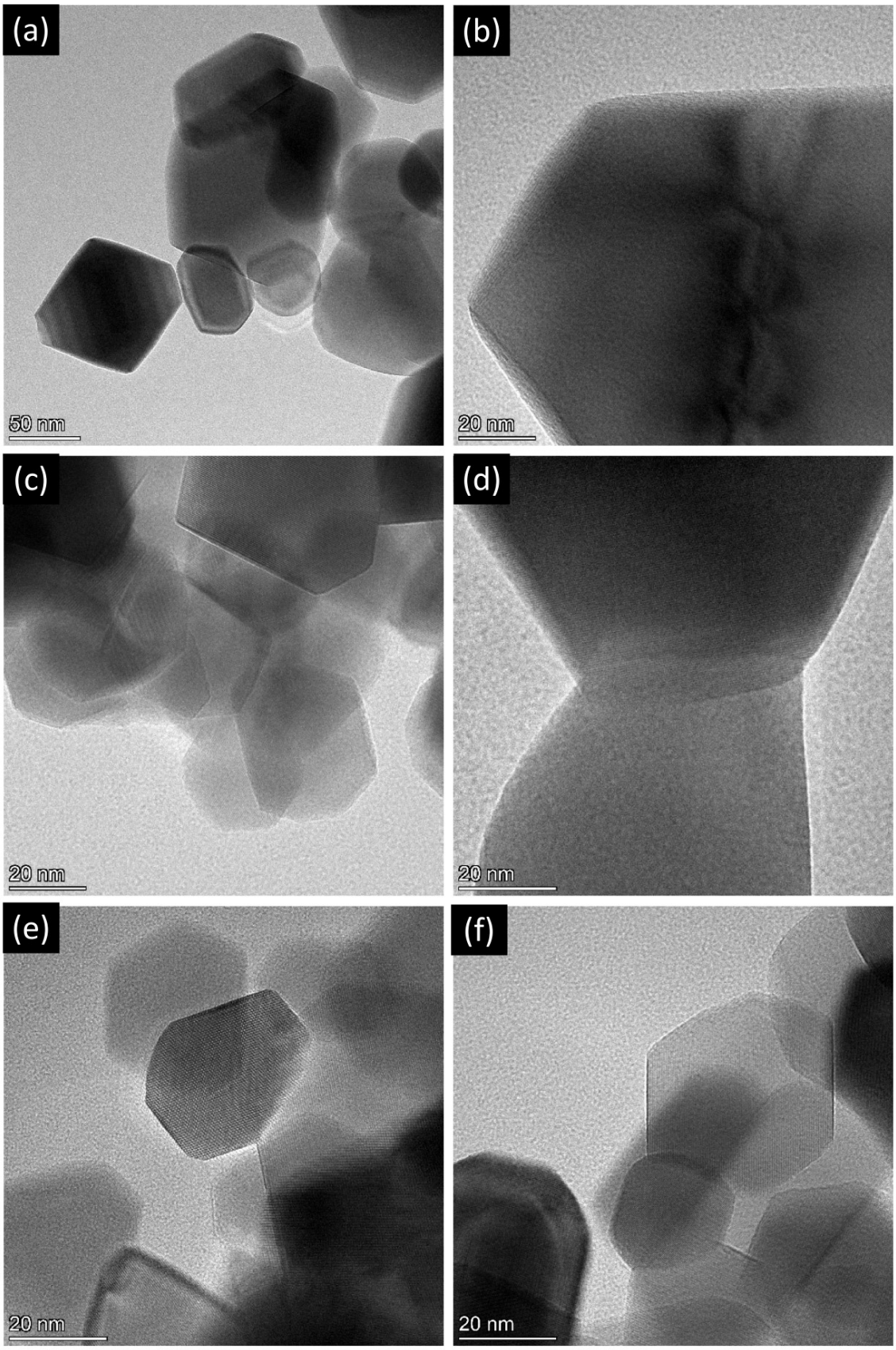

Fig. S5 HRTEM images of samples (a,b) CoNi, (c,d) CoZn and (e,f) NiZn.

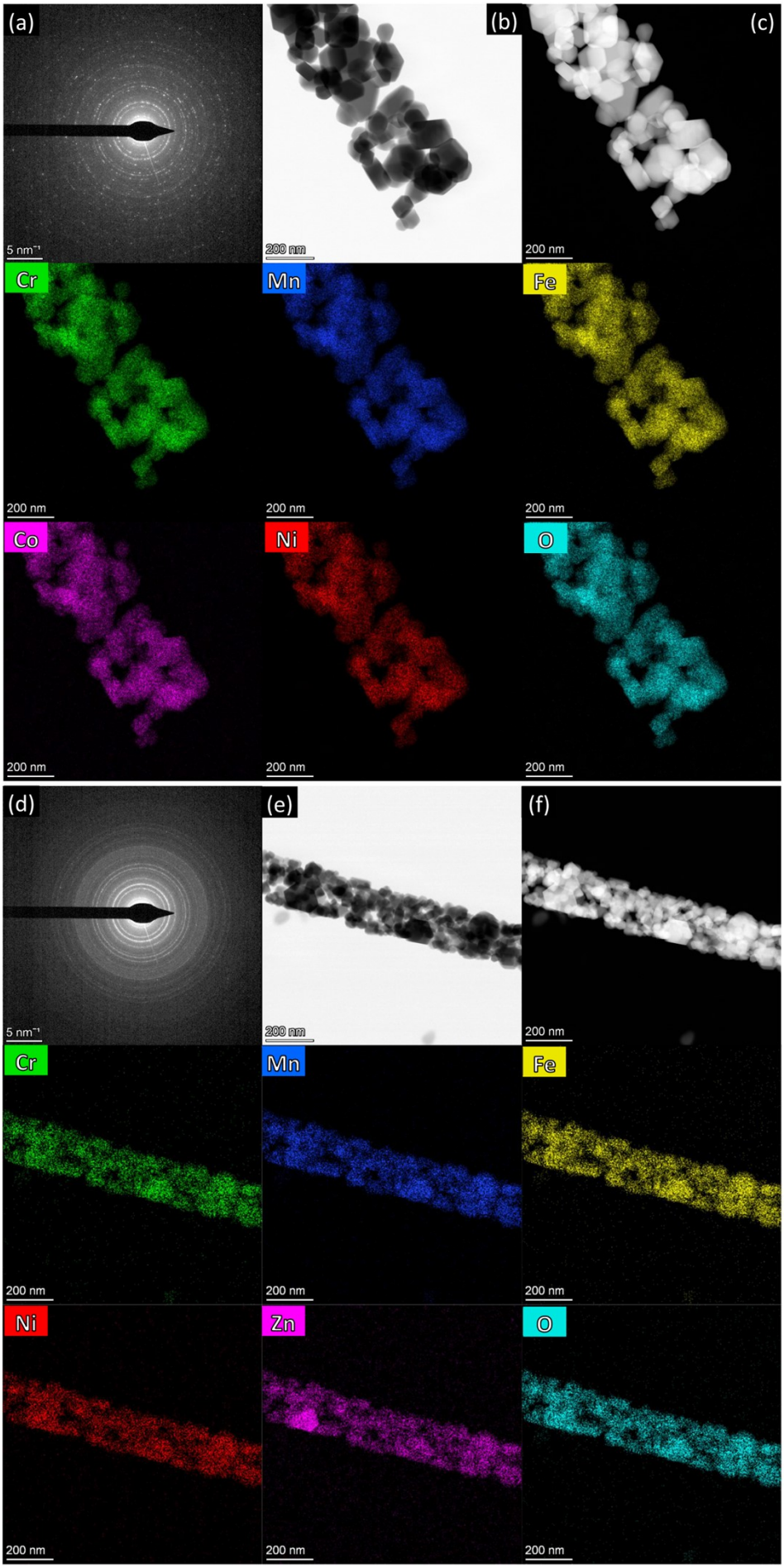

Fig. S6 (a,d) SAED patterns for (b,e) isolated NFs and (c,f) STEM/EDX elemental maps. The shown data refer to samples (a–c) CoNi and (d–f) NiZn.

Table S2. Outer and inner diameters of the NFs as resulting from statistical and projection analysis of the HRTEM images, along with the calculated shell thickness.

Sample	CoNi	CoZn	NiZn
Outer NF diameters / nm	250–450	170–280	160–240
Inner NF diameters / nm	70–270	120–180	60–100
Shell thickness / nm	60–90	40–60	50–80

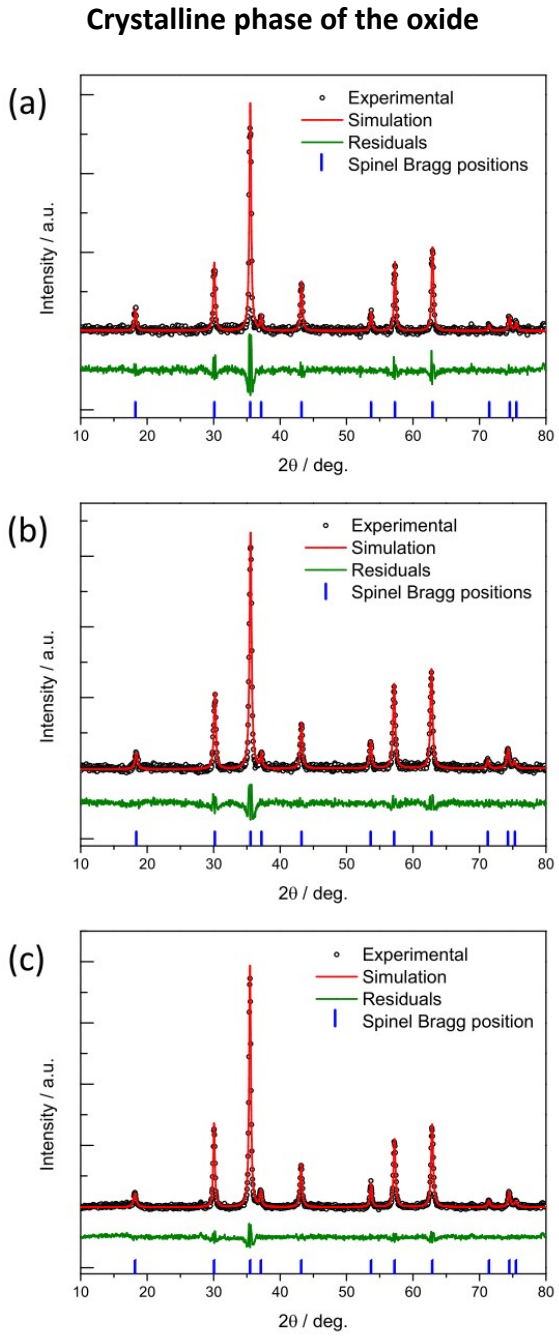

Fig. S7 Rietveld refinements. The cases shown refer to samples (a) CoNi, (b) CoZn and (c) NiZn.

Surface composition of HESO-NFs and oxidation states of cations

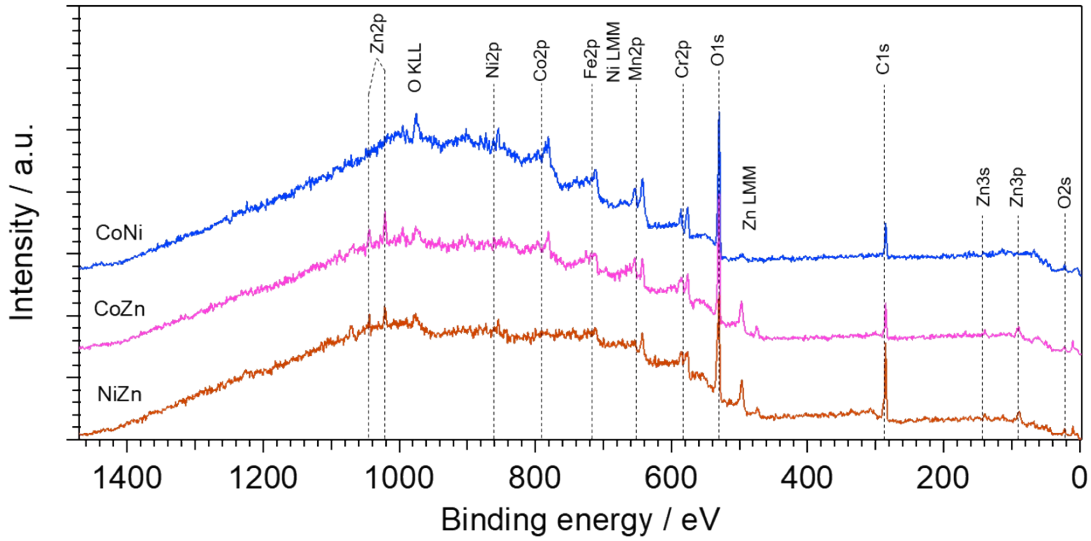

Fig. S8 XPS survey analyses of the investigated HEOs.

Table S3. Surface elemental composition of samples CoNi, CoZn and NiZn.

Sample	Cr / at.%	Mn / at.%	Fe / at.%	Co / at.%	Ni / at.%	Zn / at.%	O / at.%
CoNi	5.71	7.14	2.79	3.10	2.45	--	78.82
CoZn	6.09	8.06	3.23	3.23	--	6.57	72.83
NiZn	8.45	7.99	1.52	--	2.37	5.07	74.61

Table S4. Chromium and oxygen relative composition in samples CoNi, CoZn and NiZn.

Sample	Cr		O		
	Cr(III) / at.%	Cr(VI) / at.%	O_L[a] / at.%	O_V[b] / at.%	ads. O / at.%
CoNi	82.13	17.87	65.13	19.89	14.98
CoZn	88.39	11.61	70.77	13.22	16.01
NiZn	81.08	18.92	57.58	13.97	28.44

[a] Lattice O^{2-} ions (O_L).

[b] Native defects of O^{2-} vacancies (O_V).

Phase purity of the oxide and inversion degree of the spinel phase

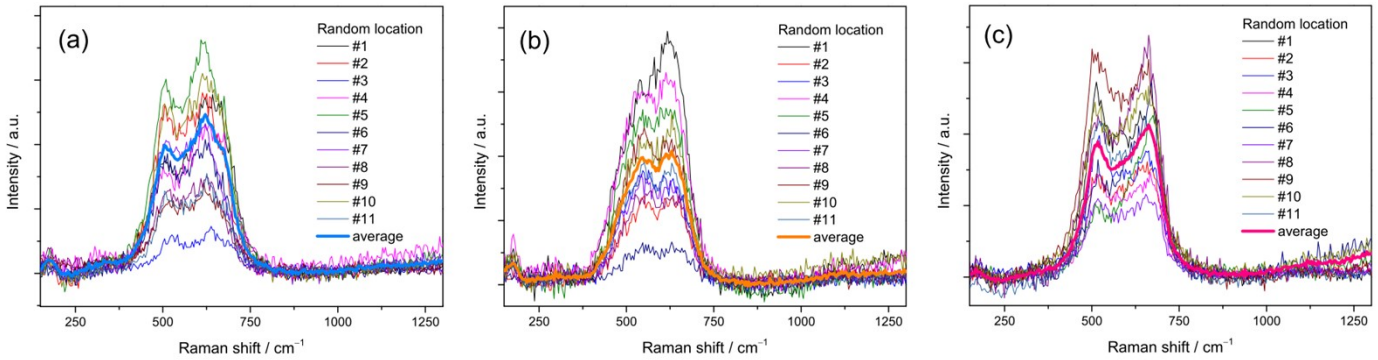

Fig. S9 Micro-Raman spectra, as measured at different random locations, within each specimen. The shown data refer to samples (a) CoNi, (b) CoZn and (c) NiZn.

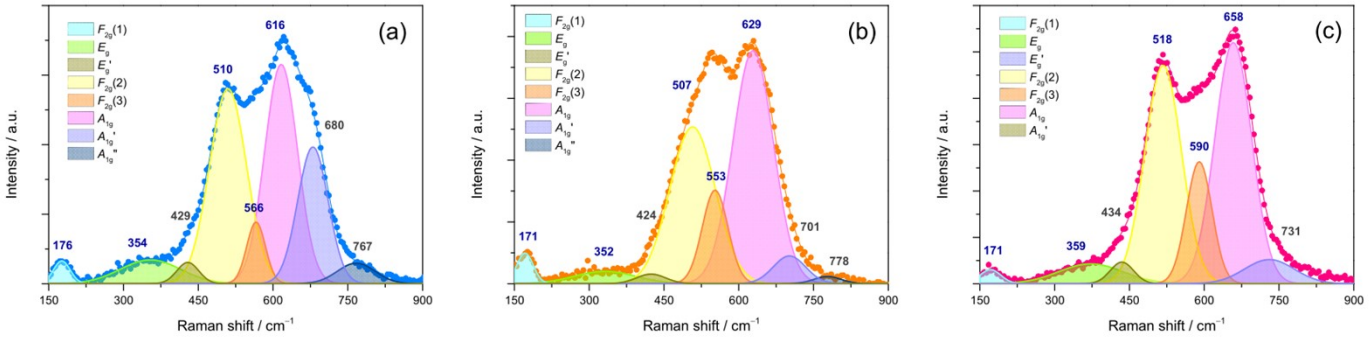

Fig. S10 (a–c) Fits of the micro-Raman spectra to Gaussian bands. The shown data refer to samples (a) CoNi, (b) CoZn and (c) NiZn.

Monte Carlo calculation of the magnetization of HESO-NFs

For the purpose of calculating magnetization, we consider the HESO-NFs as a collection of formula units (FUs) $M_1^{(8a)}M_2^{(16d)}M_3^{(16d)}O_4$, where ion M_1 occupies the 8a site and ions M_2 and M_3 occupy the 16d sites. We consider $N = 10^6$ independent FUs and randomly occupy the 8a and 16d sites consistently with the cation distributions in Table 1 of the main text. The magnetic moment of each cation was taken from Ref. 8. The effective magnetic moment per FU is calculated as

$$\mu_{eff} = \sqrt{\frac{1}{N}\sum_{i=1}^{N}\sum_{j=1}^{3}\mu_{i,j}^2}$$

where $\mu_{i,j}$ is the magnetic moment of the cation occupying site *j* in the *i*-th realization of the FU. The corresponding Curie constant per FU *C* is $C = N_A\,\mu_{eff} / (3\,k_B)$, where N_A is Avogadro number and k_B is Boltzmann constant. The molar saturation magnetization of the 8a and 16d sites is

$$M^{(8a)} = N_A\frac{1}{N}\sum_{i=1}^{N}\sum_{j\in 8a}\mu_{i,j}\,,\ M^{(16d)} = N_A\frac{1}{N}\sum_{i=1}^{N}\sum_{j\in 16d}\mu_{i,j}$$

The saturation magnetization in the paramagnetic (PM) region is

$$M_{PM} = M^{(16d)} + M^{(8a)}$$

and the saturation magnetization for *collinear* (Néel type) ferrimagnetic (FIM) order is

$$M_{FIM} = M^{(16d)} - M^{(8a)}$$

Fitting the saturation approach model to high field magnetization data

The standard model for the magnetic saturation approach of ferrimagnetic powders[7] is $M = M_{sat}(1–A/H–B/H^2) + \chi_p H$ where M_{sat}, *A*, *B*, and the the linear (paramagnetic) susceptibility χ_p are parameters to be optimized. The optimization was carried out by minimizing the sum of the absolute residuals by a simplex procedure using the data points with $H \geq H_{min}$ ($H_{min} = 10^4$ Oe, exception is $H_{min} = 2\cdot10^4$ Oe for CoZn at 5 K. It turned out that the B/H^2 term was not statistically significant and good fits were obtained with the simpler formula $M = M_{sat}(1–A/H) + \chi_p H$.

Table S5 summarizes the best-fit parameters, and the experimental and best-fit magnetization are compared in Figure S11.

Table S5. Optimized parameters from fitting the simplified saturation approach model $M = M_{sat}(1–A/H) + \chi_p H$ to high-field isotherm magnetization data.

	***T* (K)**	M_{sat} (emu g^{-1})	$10^4\,\chi_p$ (emu g^{-1} Oe^{-1})	*A* (Oe)	*S* (emu g^{-1}) [a]
CoNi	5	39.3	0.15	437	0.0071
	50	37.4	0.18	365	0.0266
	100	31.9	0.22	341	0.0101
	200	20.0	0.28	323	0.0109
	300	9.6	0.36	402	0.0097
CoZn	5	27.9	0.72	3813	0.1269
	20	23.4	1.23	1682	0.0510
	50	21.8	1.22	1458	0.0439
	150	3.68	1.55	5347	0.0487
	300		0.54	13690	0.0046
NiZn	5	14.8	0.51	896	0.0203
	20	14.7	0.62	758	0.0123
	50	14.6	0.57	587	0.0491
	150	9.6	0.44	1125	0.0209
	300	0.7	0.45	3180	0.0291

[a] *S* is the sum of the absolute residuals divided by the number of data points used in the fitting procedure.

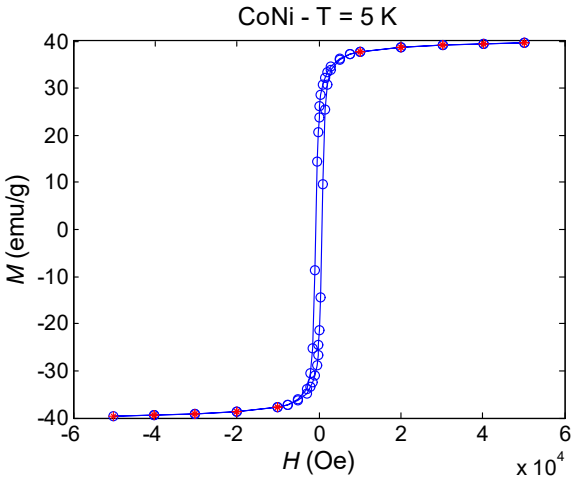
CoNi - T = 5 K
M (emu/g)
H (Oe)
x 10^4

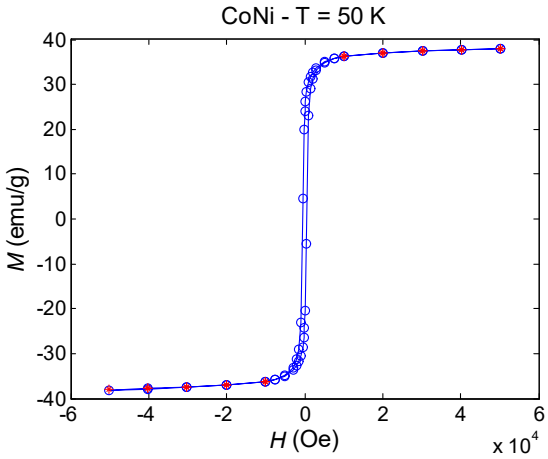
CoNi - T = 50 K
M (emu/g)
H (Oe)
x 10^4

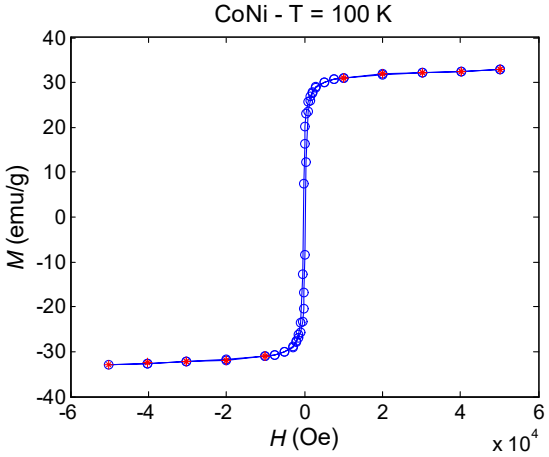
CoNi - T = 100 K
M (emu/g)
H (Oe)
x 10^4

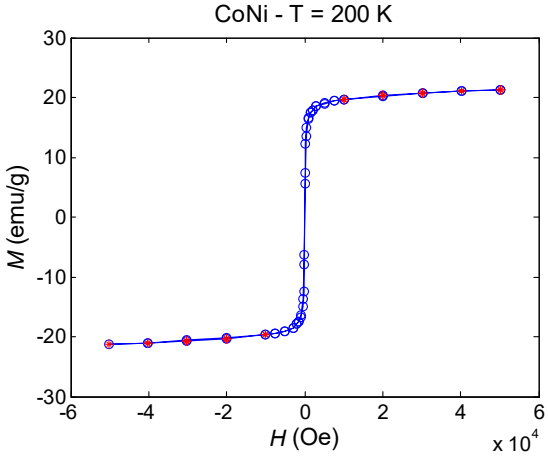
CoNi - T = 200 K
M (emu/g)
H (Oe)
x 10^4

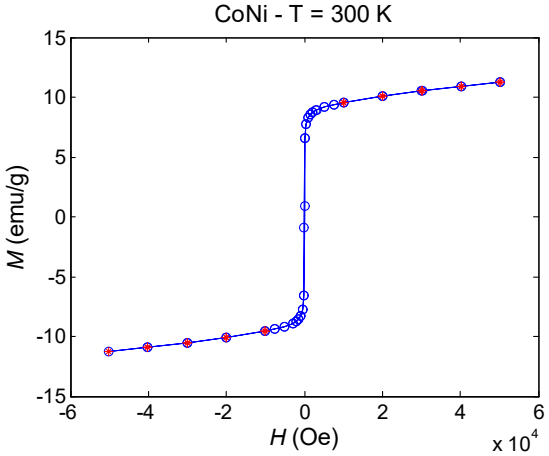
CoNi - T = 300 K
M (emu/g)
H (Oe)
x 10^4

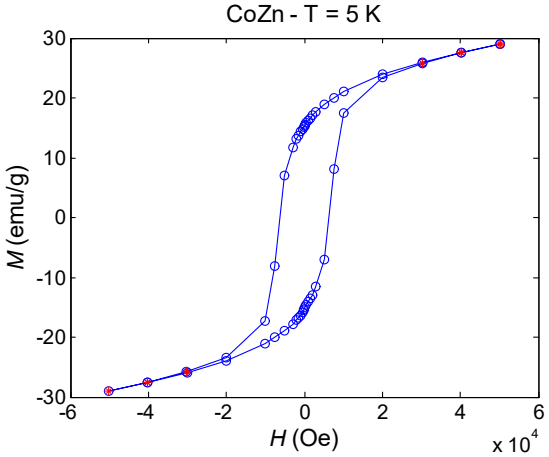
CoZn - T = 5 K
M (emu/g)
H (Oe)
x 10^4

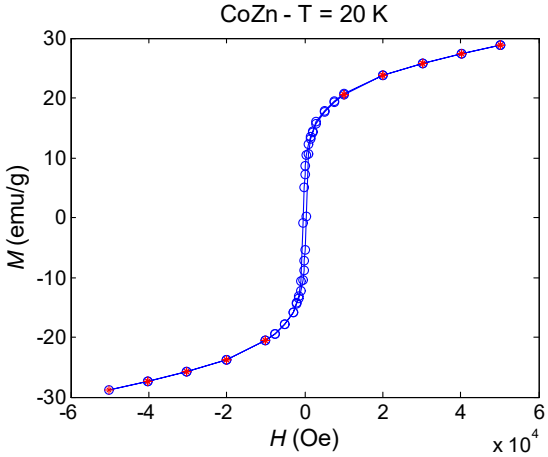
CoZn - T = 20 K
M (emu/g)
H (Oe)
x 10^4

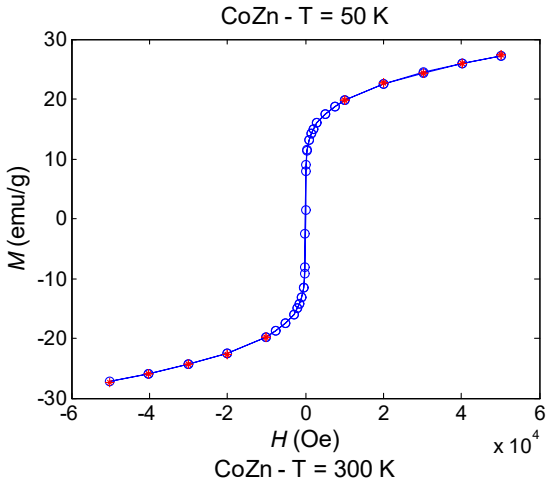
CoZn - T = 50 K
M (emu/g)
H (Oe)
x 10^4

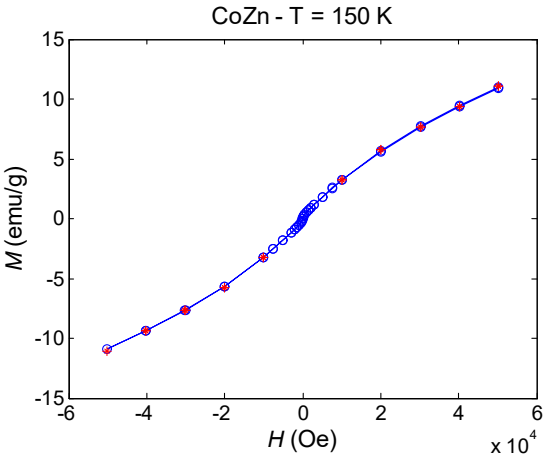
CoZn - T = 150 K
M (emu/g)
H (Oe)
x 10^4

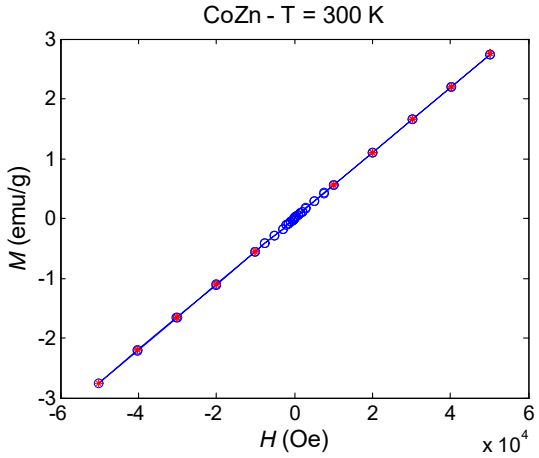
CoZn - T = 300 K
M (emu/g)
H (Oe)
x 10^4

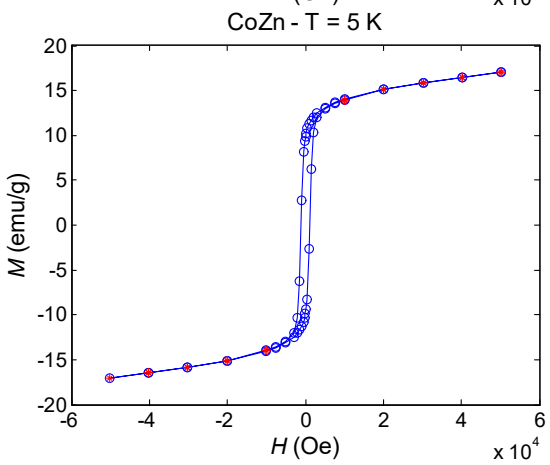
CoZn - T = 5 K
M (emu/g)
H (Oe)
x 10^4

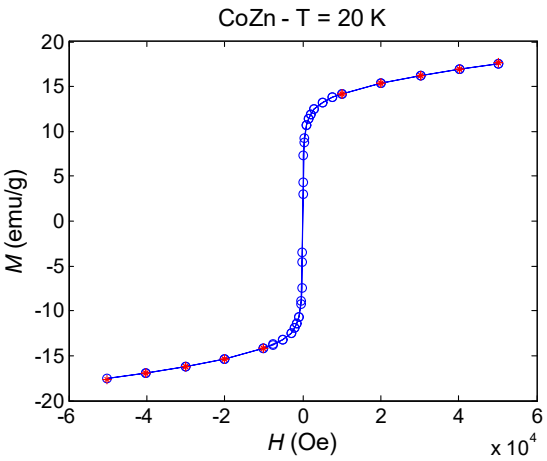
CoZn - T = 20 K
M (emu/g)
H (Oe)
x 10^4

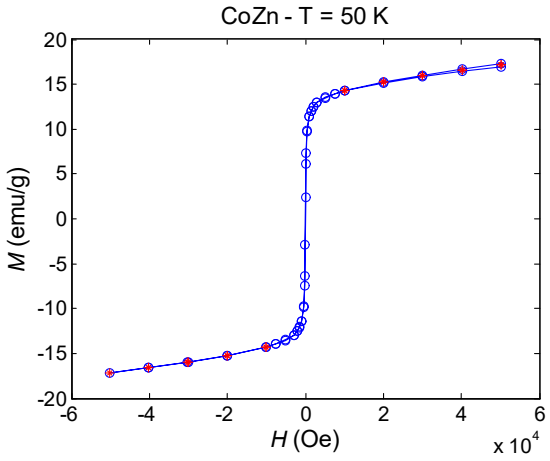
CoZn - T = 50 K
M (emu/g)
H (Oe)
x 10^4

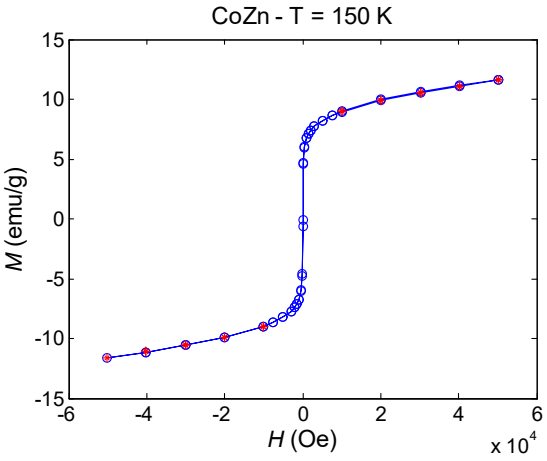
CoZn - T = 150 K
M (emu/g)
H (Oe)
x 10^4

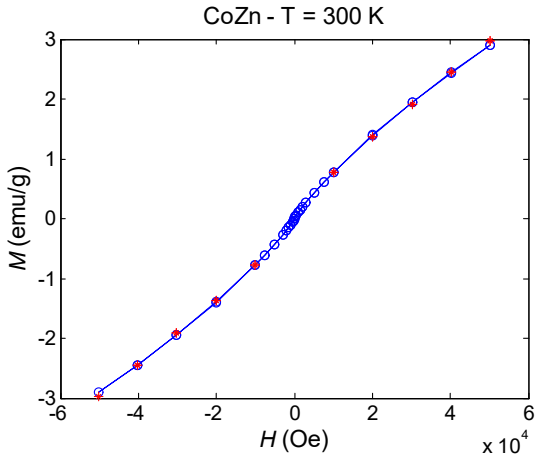

Fig. S11. Fit of the simplified saturation approach model $M = M_{sat}(1–A/H) + \chi_p H$ to high-field isotherm magnetization data. The experimental data (blue) are in good agreement with the saturation approach model (red asterisks).

Calculation of the Helmholtz free energy for cation distributions

In spinel oxides, cations occupy tetrahedral 8a sites and octahedral 16d sites. All cations (Cr, Mn, Fe, Co, Ni, Zn) have a preference for the 16d sites.[9,10] The excess octahedral stabilization energy can be found in Table S6.

Table S6. Crystal field excess octahedral stabilization energy (*E*, kJ/mol) for transition metal cation in oxides.[10]

	2+	3+
Cr		158
Mn	0	95
Fe	17	0
Co	31	16 [b]
Ni	86	27 [b]
Zn	0	

[b] Values estimated from the stabilization energy of the divalent cation, using the well-known formulae from crystal field theory $E(Co^{3+}) = (1/2)\ E(Co^{2+})$ and $E(Ni^{3+}) = (12/38)\ E(Ni^{2+})$.

For a given FU composition $(M_1)_{(8a)}(M_2M_3)_{(16d)}O_4$, the excess octahedral stabilization energy is $E = E(M_2) + E(M_3)$. In the case that cation randomization is complete, i.e., the cations are homogeneously distributed over the 8a and 16d sites, the excess octahedral stabilization ΔE^{FU} is the average over all possible FU compositions (Table S6).

We can also conceive that the cations are homogeneously distributed within the 8a and 16d sites bit that they distribute between the 8a and 16d sites in order to maximize the excess octahedral stabilization energy, under the constraint of electroneutrality. Such distributions can be found in the main text. The corresponding average excess octahedral stabilization are larger by ≈60 kJ/mol than those for the completely random distribution (Table S7).

Table S7. Excess octahedral stabilization energy (Δ*E*, kJ/mol), configurational entropy (J/mol K) and Helmholtz free energy (Δ*F*, kJ/mol) at 1173 K for completely random and intrasite-random cation distributions.

	Completely random			Intrasite-random		
NF	<*E*>	*S*	*F*	<*E*>	*S*	*F*
CoNi	146	40	–193	210	24	–238
CoZn	112	40	–159	167	24	–195
NiZn	128	40	–175	192	24	–220

The corresponding Helmholtz free energy $F = -\langle E\rangle - TS_{config}$ are calculated using the configurational entropy

$$S_{config}^{FU} = -R\left(\sum_i x_i^{(8a)} \ln x_i^{(8a)} + 2\sum_i x_i^{(16d)} \ln x_i^{(16d)}\right)$$

and the highest calcination temperature T = 1173 K. The Helmholtz free energy for the intrasite-random distribution is lower by ≈40 kJ/mol than those for the completely random distribution. The former is thus strongly favored at the highest calcination temperature, and we expect that in our NFs cations are distributed following the intrasite-random distribution and satisfy the cation preferences for 16d sites.

The two distribution models have equal Helmholtz free energy at temperature well above 3000 K. Thus, it seems very unlikely that spinel oxides with a completely random distribution of cations from the late part of the first transition (Cr-Zn) can be synthesized by thermal methods.

Table S8. Magnetic lengths of spinel oxides.

Material	D_{sd} / nm	D_{coh} / nm	D_b / nm [a]	Ref.
Fe_3O_4	75	48	27	[11]
$CoFe_2O_4$	320	52	11	[11]
$CoCr_2O_4$	$12\cdot10^3$	660	45	[12]

[a] Superparamagnetic blocking diameter at 400 K.

Notes and references

1 K. E. Sickafus, J. M. Wills, N. W. Grimes, *J. Am. Ceram. Soc.*, 1999, **82**, 3279–92.
2 A. Ponti, M. H. Raza, F. Pantò, A. M. Ferretti, C. Triolo, S. Patanè, ... S. Santangelo, *Langmuir*, 2020, **36** (5), 1305–1319.
3 M. J. Hÿtch, *Microsc. Microanal. Microst.*, 1997, **8**, 41−57.
4 J. L. Rouvière, E. Sarigiannidou, *Ultramicroscopy*, 2005, **106**, 1−17.
5 D. Briggs, M. P. Seah, *John Wiley & Sons*: New York, 2nd ed. 1990.
6 D. A. Shirley, *Phys. Rev. B*, 1972, **5**, 4709−4714.
7 X. Batlle, M. García del Muro, J. Tejada, H. Pfeiffer, P. Görnert, E. Sinn, *J. Appl. Phys.*, 1993, **74** (5), 3333–3340.
8 K. H. J. Buschow, F. R. de Boer, Physics of Magnetism and Magnetic Materials. New York, NY, USA: Springer, 2003.
9 A. F. Wells, Structural Inorganic Chemistry. Oxford (UK): Clarendon Press, 2012.
10 A. R. West, Solid State Chemistry and Its Applications. Second edition, Student edition. Chichester, West Sussex, UK: Wiley, 2014.
11 J. M. D. Coey, J. M. D. Magnetism and Magnetic Materials; Cambridge University Press: Cambridge (UK), 2013.
12 W. J. Li, C. J. Wang, X. M. Zhang, M. Irfan, U. Khan, Y. W. Liu, X. F. Han, *Nanotechnology*, 2018, **29** (24), 245601.